LETTER

https://doi.org/10.1038/s41586-019-1189-0

Chang'E-4 initial spectroscopic identification of lunar far-side mantle-derived materials

Chunlai Li[1]*, Dawei Liu[1], Bin Liu[1], Xin Ren[1]*, Jianjun Liu[1]*, Zhiping He[2], Wei Zuo[1], Xingguo Zeng[1], Rui Xu[2], Xu Tan[1], Xiaoxia Zhang[1], Wangli Chen[1], Rong Shu[2], Weibin Wen[1], Yan Su[1], Hongbo Zhang[1] & Ziyuan Ouyang[1,3]

Over 60 years of spacecraft exploration has revealed that the Earth's Moon is characterized by a lunar crust[1] dominated by the mineral plagioclase, overlying a more mafic (richer in iron and magnesium) mantle of uncertain composition. Both crust and mantle formed during the earliest stages of lunar evolution when late-stage accretional energy caused a molten rock (magma) ocean, flotation of the light plagioclase, sinking of the denser iron-rich minerals, such as olivine and pyroxene, and eventually solidification[2]. Very large impact craters can potentially penetrate through the crust and sample the lunar mantle. The largest of these craters is the approximately 2,500-kilometre-diameter South Pole-Aitken (SPA) basin[3] on the lunar far side. Evidence obtained from orbiting spacecraft shows that the floor of the SPA basin is rich in mafic minerals[4], but their mantle origin is controversial and their in situ geologic settings are poorly known. China's Chang'E-4 lunar far-side lander recently touched down in the Von Kármán crater[5,6] to explore the floor of the huge SPA basin and deployed its rover, Yutu-2. Here we report on the initial spectral observations of the Visible and Near Infrared Spectrometer (VNIS)[7] onboard Yutu-2, which we interpret to represent the presence of low-calcium (ortho)pyroxene and olivine, materials that may originate from the lunar mantle. Geological context[6] suggests that these materials were excavated from below the SPA floor by the nearby 72-km-diameter Finsen impact crater event, and transported to the landing site. Continued exploration by Yutu-2 will target these materials on the floor of the Von Kármán crater to understand their geologic context, origin and abundance, and to assess the possibility of sample-return scenarios.

The detailed nature of the lunar mantle has eluded investigators since the Moon was first found to be differentiated and the crust to have formed by late-stage accretional energy and plagioclase flotation—a process different from the one that formed Earth's crust[2]. However, the initial composition and structure of the lunar mantle and how these constrain models of the formation and evolution of the Moon remain unknown. No direct evidence (such as unequivocal samples of the lunar mantle) was found in material returned by the Apollo and Luna missions[8,9]. Indirect information has come from Apollo seismic experiments and the nature of mare basalts sourced from the lunar mantle, but fundamental questions remain[8]. Predictions ranged from a mantle dominated by olivine, an orthopyroxenite with trace amounts of olivine, or some other combination of these component minerals[8]. After recognizing that impact craters form 'drill holes' into the lunar subsurface, investigators turned to orbital elemental and mineralogical measurements to probe the nature of the lunar crust and mantle, finding evidence of stratification in the lunar crust[10]. Evidence of the presence of olivine—a known major component of planetary mantles—was surprisingly sparse on the lunar surface; the mineral was found mostly around impact basins of moderate to large size, but even there it was not abundant or widespread[11]. Attention turned to the largest and oldest impact basin, the about 2,500-km-diameter SPA basin, which is located on the lunar far side[12,13]. A basin this large would be the best candidate to have penetrated below the crust and deep into the lunar interior, excavating lunar mantle and distributing it on the surface in the form of ejecta and impact melt deposits. Recent refinement (downward) of estimates of lunar crustal thickness from the GRAIL mission[1] further supported the likelihood that the SPA impact should have excavated olivine-rich mantle material. Orbital remote-sensing measurements revealed that, despite not being flooded by mare basalts, the SPA interior was clearly more iron-rich than the lunar highland[13]. In addition, although there is abundant evidence of the presence of pyroxene[12] in the SPA interior, olivine was found in only two places, inside the Schrödinger basin and the Zeeman crater—both later events superposed near the edges of the SPA interior[14]. The lack of evidence of widespread and abundant olivine in the largest impact basin on the Moon led to an alternative interpretation: that the SPA basin event was probably an oblique impact[15], excavating pyroxene-rich lower-crust material (norites)[3,12] instead of olivine-bearing mantle material. The picture was further complicated by the growing awareness that large impact basins would produce huge quantities of impact melt, which is predicted to pond and possibly undergo differentiation in the basin interior[16,17]. What would these products look like and how can we distinguish these from samples of the lunar mantle? Furthermore, how might emplacement of post-SPA-basin maria and cryptomaria[18] influence remote-sensing data?

Recent developments in impact-basin hydrocode modelling enabled a more detailed prediction of the nature of an SPA-scale basin-forming event[19,20]. These models show that the SPA event should have penetrated to depths of several hundred kilometres, well below the crustal thickness estimated by the GRAIL data[1], and would have clearly excavated mantle material and redistributed it on the surface within and in the vicinity of the SPA basin. However, the absence of abundant olivine in the SPA interior remains a conundrum. Could the predictions of an olivine-rich lunar mantle[8,9] be incorrect? A partial solution to this problem has been recently proposed[20]: perhaps the mantle was composed predominantly of orthopyroxine, not olivine. Could orthopyroxene[4] actually be the dominant material in the upper lunar mantle and olivine a minor component?

These questions were of such fundamental importance that they were prominently featured in documents reporting national space exploration strategies[21,22]. However, exploration infrastructure technology had confined the several dozen in situ lunar missions to land on the lunar near side. Further insight required in situ analyses and sample return from the floor of the SPA basin, on the lunar far side. In an effort to address these fundamental questions, the Chinese Lunar Exploration Program (CLEP) developed and implemented the QueQiao relay satellite to facilitate lunar far-side in situ surface exploration and sample-return missions.

Such a mission[5] is Chang'E-4, which was targeted at the floor of the SPA basin. Paramount in the selection of the landing site were scientific goals and objectives, as well as landing safety. To have the highest likelihood of sampling lunar-mantle material[6], the landing site was chosen

[1]Key Laboratory of Lunar and Deep Space Exploration, National Astronomical Observatories, Chinese Academy of Sciences, Beijing, China. [2]Key Laboratory of Space Active Opto-Electronics Technology, Shanghai Institute of Technical Physics, The Chinese Academy of Sciences, Shanghai, China. [3]Institute of Geochemistry, Chinese Academy of Sciences, Guiyang, China. *e-mail: licl@nao.cas.cn; renx@nao.cas.cn; liujj@nao.cas.cn

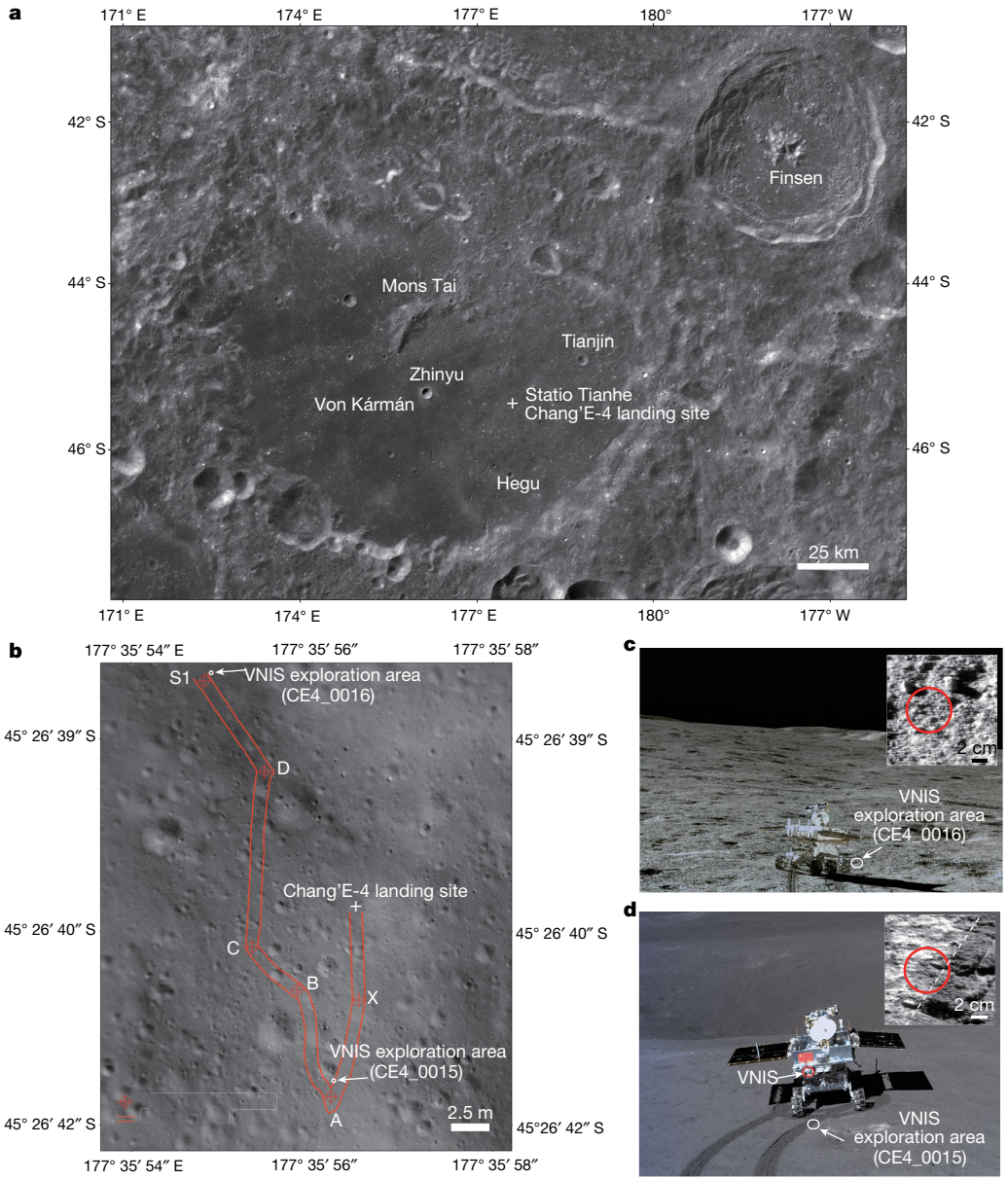

Fig. 1 | Locations of the Chang'E-4 landing site and the VNIS measurements. a, The Chang'E-4 landing site on a 7-m-resolution Chang'E-2 Digital Orthophoto Map. **b**, Yutu-2 rover traverse map and location of VNIS detection points S1 (CE4_0016) and A (CE4_0015) during the first lunar day; red lines are Yutu-2 wheel tracks. **c**, **d**, Images of the VNIS conducting spectral detection at points S1 and A on the lunar surface. The images were acquired by the Terrain Camera[5]. Insets, 600-nm-band images of points S1 and A, obtained by the VNIS. The red circles show the field view of the SWIR detector, and the white dashed line is the boundary between the rover wheel track and the lunar surface.

on the relatively smooth mare floor of the post-SPA-basin Von Kármán crater (diameter of about 186 km). The geologic setting of the landing site[6] is a region of impact craters superposed on the floor of the SPA basin (the 225-km-diameter Von Kármán M crater and the 245-km-diameter Leibnitz crater), and other nearby craters that are likely to deliver SPA-basin-subfloor material to the landing site. The youngest of these is the 72-km-diameter crater Finsen, which is located to the northeast of the landing site and clearly delivers ejecta to the landing-site region. The fact that the central peaks of Finsen have provided the most prominent and purest detection of orthopyroxene in the SPA basin[23] strongly suggests that mantle material has been delivered to the site by the Finsen cratering event. Thus the regionally smooth Von Karman floor mare deposits enhance landing safety, and the extensive ejecta delivered by Finsen and other nearby deeply excavating post-SPA craters provide multiple possible samples of lunar mantle[6].

Chang'E-4 successfully landed in the Von Kármán crater of the SPA basin at 10:26 (UTC+8) on 3 January 2019. The Chang'E-4 landing site (called Statio Tianhe) is 177.5991° E, 45.4446° S, with a −5,935-m surface elevation (relative to a 1,737.4-km-radius lunar spheroid). The VNIS[7] onboard the Yutu-2 rover enabled the first in situ reflectance measurements of the far side of the Moon. The VNIS acquires hyperspectral reflectance data at wavelengths of 450–2,400 nm with spectral resolutions of 2.4–6.5 nm for visible/near-infrared (VIS/NIR) and 3.6–9.6 nm for the short wave infrared spectrometer (SWIR; see Methods).

The radiance spectra of two sites adjacent to the lander (Fig. 1) were collected during the first lunar day. These radiance spectra were first divided by the solar irradiance and smoothed to obtain the reflectance factor (REFF) (Fig. 2a). Continuum-removal and parabola fits were then applied to acquire an accurate absorption-band centre for the two reflectance spectra (Fig. 2b; see Methods).

The two spectra obtained by Chang'E-4 are obviously different from Chang'E-3 spectra of mare soils in Mare Imbrium[24] (Fig. 2) and those of mare samples measured by the Lunar Soils Characterization

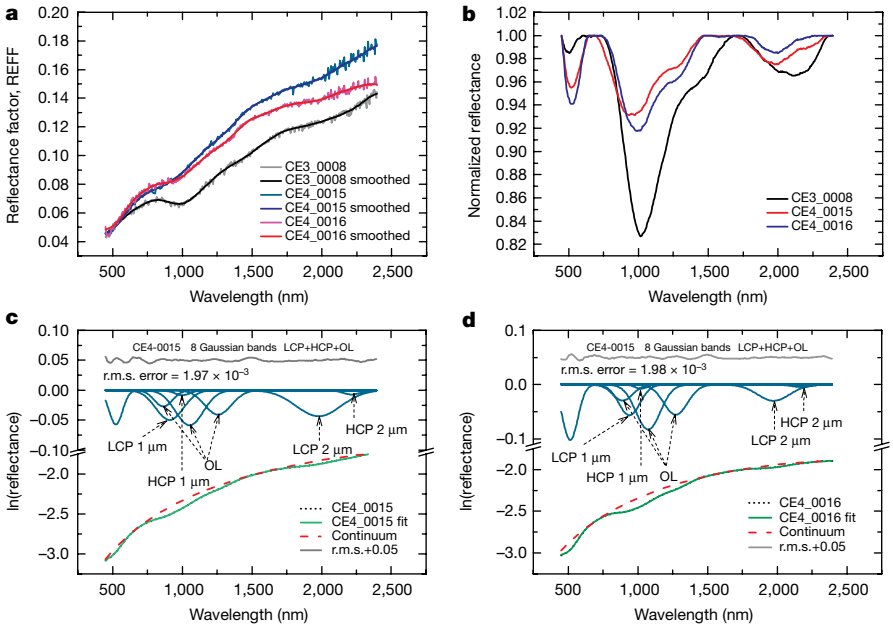

Fig. 2 | Chang'E-4 reflectance spectra acquired by the VNIS during the first lunar day. a, Reflectance (REFF) spectra obtained by Chang'E-4 VNIS (CE4_0015 and CE_0016) and the Chang'E-3 VNIS detection point (CE3_0008). **b**, Continuum-removed spectra of **a**. **c**, **d**, MGM-fitting results for CE4_0015 and CE4_0016 using endmember LCP, HCP and olivine.

Consortium (LSCC; Extended Data Fig. 1a). They are characterized by an attenuated absorption-band strength and a red-sloped continuum, indicating a stronger space weathering effect[25,26] than that of the Chang'E-3 samples. In addition, the centres of the 1-μm and 2-μm absorption bands in the Chang'E-4 spectra move to shorter wavelengths, showing apparent spectral features of low-Ca pyroxene (LCP) and olivine. The overall spectral shape and absorption-band positions are more similar to those of lunar highland materials (Extended Data Fig. 1b). These results suggest that the materials at the Chang'E-4 landing site are enriched in mafic components distinct from mare basalt.

The characteristic 1-μm and 2-μm absorption features of the two VNIS observations are attributed to the presence of pyroxene-bearing lithologies in the soils of the Chang'E-4 landing site. We plotted the positions of the 1-μm and 2-μm bands of the two spectra (Extended Data Fig. 2) on the trend line (Fig. 3) defined by pyroxene of varying compositions (from Mg-rich LCP to Ca- and Fe-rich pyroxene)[4] to further classify the type of pyroxene and determine whether other possible minerals might exist within the Chang'E-4 landing site. Although CE4_0015 and CE4_0016 have a weak 2-μm absorption, it can still be seen that the centres of their 2-μm absorption bands are below 2,000 nm, suggesting that the materials at the landing site exhibit an LCP signature[27,28] (CE4_0015 and CE4_0016 represent the 15th and 16th navigation points of the Yutu-2 rover, respectively, where the two spectra were acquired). However, the 1-μm and 2-μm-band positions of the two Chang'E-4 spectra do not strictly follow the trend; the 1-μm-band position of CE4_0015 is slightly above the pure-pyroxene trend line, and the 1-μm-band position of CE4_0016 shows a large deviation. One plausible reason is that CE4_0016 has a higher abundance of olivine, in addition to LCP. The strong 1,050-nm absorption band of olivine could result in a shift of the 1-μm-band position of CE4_0016 towards longer wavelengths while not affecting its 2-μm-band position. The wider 1-μm absorption band (Fig. 2b) of the Chang'E-4 continuum-removed spectra (from which the base curve has been removed to emphasize the absorption features of the reflectance spectra) relative to that of pure pyroxene could also be due to the presence of olivine. In addition, these two Chang'E-4 spectra show an apparently weaker 2-μm absorption depth than that at 1 μm, as well as an absorption feature around 1,250 nm, which could be attributed to olivine. Although the two spectra exhibit similar 2-μm absorption-band positions (1,985.9 nm and 1,984.9 nm), CE4_0016 shows a deeper and slightly more asymmetric absorption relative to CE4_0015, suggesting a higher abundance of olivine within CE4_0016 than CE4_0015.

The modified Gaussian model (MGM) was applied to deconvolve the two spectra of the Chang'E-4 landing site to constrain the minerals present and estimate their relative amounts[29,30]. Four different groups of mineral combinations were used in the MGM deconvolution: (1) LCP, HCP and olivine (OL); 2) LCP, HCP and plagioclase (Plag); 3) LCP and Plag; 4) LCP and OL. The results show that the continuum-removed reflectance spectra of CE4_0015 can be accurately fitted by the mineral combination of LCP + HCP + OL, with the lowest root-mean-square (r.m.s.) deviation relative to the other three groups of mineral combination (Fig. 2c, Extended Data Fig. 3). The significance test results also show that HCP + LCP + OL can achieve the best MGM

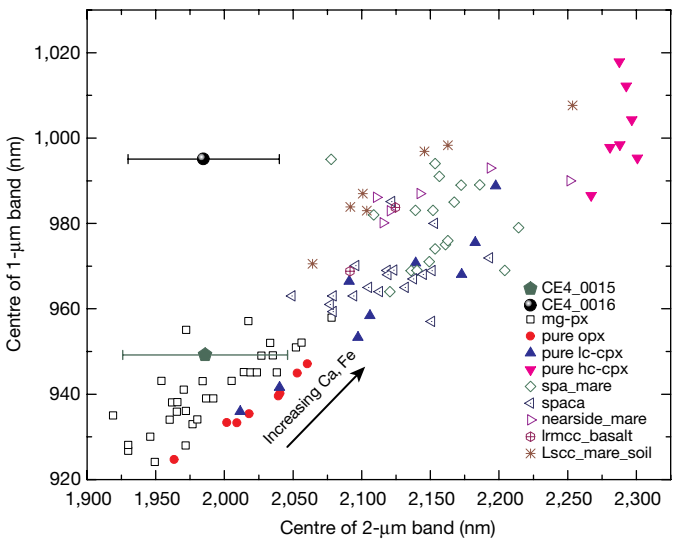

Fig. 3 | Absorption-band positions for CE_0015 and CE_0016. Positions of the 1-μm and 2-μm bands of the two Chang'E-4 spectra compared with the trend line defined by pyroxene of varying compositions (data are from figure 8b of ref. [4]; annotation as in ref. [4]). The solid green polygon and black circle represent CE4_0015 and CE4_0016, respectively. The green and black error bars show the wavelength range used for the 2-μm absorption parabola fitting.

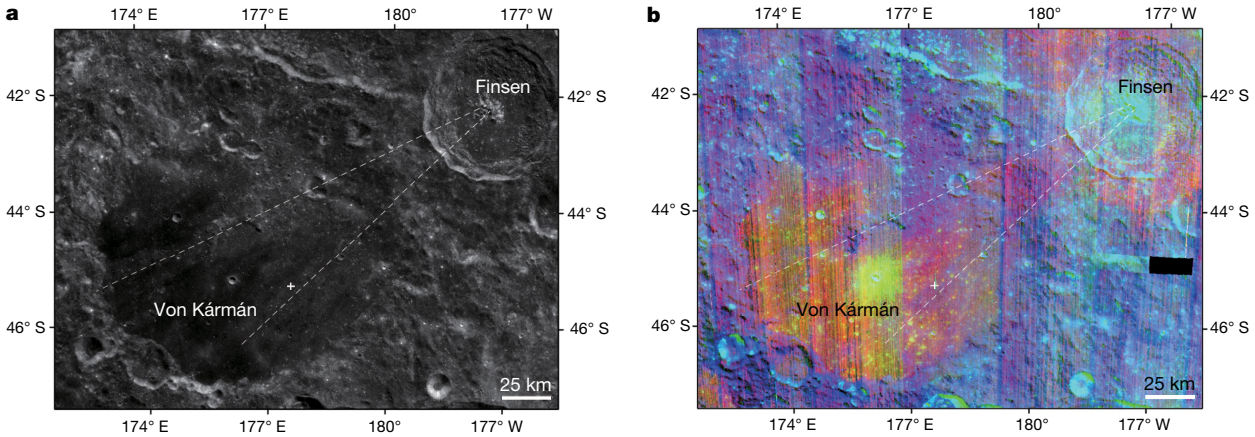

Fig. 4 | Distribution of Finsen ejecta in the Von Kármán crater. a, Chang'E-1 Digital Orthophoto Map; spatial resolution, 120 m. **b**, M^3 colour composite; R, 2-μm-band centre; G, 2-μm-band depth; B, reflectance at 1,580 nm. White dashed lines represent two major northeast–southwest ejecta rays of the Finsen crater converging towards its central peak. The white cross is the Chang'E-4 landing site, which is located on the ejecta material of the Finsen crater. The 2-μm-band centre can be used to distinguish between LCP and HCP. As the content of Fe and Ca in the pyroxene increases, the 2-μm-band centre shifts towards longer wavelengths (redder). The 2-μm-band depth indicates the relative amounts of mafic minerals. The 1,580-nm reflectance represents the brightness of the lunar soils (which can be affected by plagioclase content). LCP-bearing materials appear light blue, and HCP-bearing materials appear green.

fitting results (see Methods). Further analysis on the deconvolved 1-μm-band depth of LCP, HCP and OL suggests that for CE4_0015 the abundances for LCP:HCP:OL are 42%:10%:48% (see Methods), with the highest abundance for OL, followed by LCP and the lowest abundance for HCP. MGM deconvolution of CE4_0016 (Fig. 2d) indicates that LCP: HCP:OL 38%:7%:55%. CE4_0016 is dominated by LCP and OL and has a greater abundance of OL than CE4_0015 and a very small amount of HCP. In addition, Moon Mineralogy Mapper (M^3) spectra of materials at the Chang'E-4 landing site also exhibit spectral features of LCP[6] (Extended Data Fig. 6), in agreement with the analysis results of the Chang'E-4 data.

The Chang'E-4 landing site is located in the Von Kármán crater, which flooded after its formation by lava flows of basaltic composition[6]. However, the Chang'E-4 spectra have considerable differences from spectral features typical of mare basalts. Analysis of the Chang'E-1 image data reveals that the Chang'E-4 landing site is located in a bright northeast–southwest linear feature, which, together with another linear feature to the north, converges towards the location of the Finsen crater[6] (Fig. 4a). Therefore, we consider the Chang'E-4 landing site to have been modified by the emplacement of ejecta from Finsen[6]. The ejecta of the Finsen crater could represent deep-seated materials emplaced at the time that the SPA basin formed. Spectral analysis of M^3 data also indicates an obvious compositional difference between the bright ejecta and mare materials within the Von Kármán crater[4,6] (Fig. 4b). Moreover, extensions of these two bright linear features within the Von Kármán crater converge to the central peak of the Finsen crater, the dominant composition of which has been shown to be LCP[4,23,31]. This is consistent with what we observe in the CE4_0015 and CE_0016 data. On the basis of these analyses, we propose that materials in the immediate Chang'E-4 landing site are not dominated solely by mare basalt, but that they also contain additional mafic material ejected from the Finsen crater[6]. The materials of the Chang'E-4 landing site show a strong resemblance to those exposed in the mafic central peak of the Finsen crater and therefore could readily originate from deep-seated materials excavated at the time of the formation of the SPA basin and subsequently re-excavated by the Finsen crater event and delivered to the Chang'E-4 landing site on the floor of the Von Kármán crater.

Several studies indicate that the impact event that formed the SPA basin might not have excavated through the lunar crust and exposed the mantle material on the surface of the Moon[12,18]. Our results, however, imply that the Chang'E-4 landing site is characterized by mafic components that are dominated by LCP and olivine, with a very small amount of HCP, suggesting the presence of deep-seated material[32] from the upper mantle[20], rather than the surface mare basalts on the floor of the Von Kármán crater. Alternatively, these mafic components might originate from the base of a differentiated melt sheet[17].

In summary, we found that materials at the Chang'E-4 landing site are obviously different from most sampled mare basalts and possess mafic components that are interpreted to be dominated by LCP and olivine, with very small amounts of HCP. These may represent deep-seated materials potentially from the lunar mantle, delivered to the Chang'E-4 landing site by ejecta from the Finsen crater. Moreover, our results suggest that the predictions of an olivine-rich lunar mantle cannot be ruled out. The lunar upper mantle could be composed predominantly of both LCP and olivine, rather than simply dominated by LCP with minor olivine content. Future operations of the Chang'E-4 Yutu-2 rover will focus on validating these initial results, understanding the origin of the olivine and analysing the distribution, geologic settings, characteristics and origin of these mafic candidate mantle materials on the floor of the Von Kármán crater.

Online content

Any methods, additional references, Nature Research reporting summaries, source data, statements of data availability and associated accession codes are available at https://doi.org/10.1038/s41586-019-1189-0.

Received: 19 February 2019; Accepted: 25 March 2019;
Published online 15 May 2019.

1. Wieczorek, M. A. et al. The crust of the Moon as seen by GRAIL. *Science* **339**, 671–675 (2013).
2. Wood, J. A., Dickey, J. S., Marvin, U. B. & Powell, B. N. Lunar anorthosites and a geophysical model of the Moon. *Geochim. Cosmochim. Acta* **1**, 965–988 (1970).
3. Stuart-Alexander, D. E. *Geologic Map of the Central Far Side of the Moon I-1047* (US Geological Survey, Denver, 1978).
4. Moriarty, D. P. III & Pieters, C. M. The character of South Pole Aitken basin: patterns of surface and subsurface composition. *J. Geophys. Res. Planets* **123**, 729–747 (2018).
5. Li, C. L. et al. The Chang'e 3 mission overview. *Space Sci. Rev.* **190**, 85–101 (2015).
6. Huang, J. et al. Geological characteristics of Von Kármán crater, northwestern South Pole Aitken basin: Chang'E 4 landing site region. *J. Geophys. Res. Planets* **123**, 1684–1700 (2018).
7. He, Z. P. et al. Operating principles and detection characteristics of the visible and near-infrared imaging spectrometer in the Chang'E-3. *Res. Astron. Astrophys.* **14**, 1567–1577 (2014).
8. Wieczorek, M. A. et al. The constitution and structure of the lunar interior. *Rev. Mineral. Geochem.* **60**, 221–364 (2006).
9. Shearer, C. et al. Thermal and magmatic evolution of the Moon. *Rev. Mineral. Geochem.* **60**, 365–518 (2006).
10. Tompkins, S. & Pieters, C. M. Mineralogy of the lunar crust: results from Clementine. *Meteorit. Planet. Sci.* **34**, 25–41 (1999).

11. Yamamoto, S. et al. Possible mantle origin of olivine around lunar impact basins detected by SELENE. *Nat. Geosci.* **3**, 533–536 (2010).
12. Pieters, C. M., Tompkins, S., Head, J. W. & Hess, P. C. Mineralogy of the mafic anomaly in the South Pole-Aitken basin: implications for excavation of the lunar mantle. *Geophys. Res. Lett.* **24**, 1903–1906 (1997).
13. Prettyman, T. H. et al. Elemental composition of the lunar surface: analysis of gamma ray spectroscopy data from Lunar Prospector. *J. Geophys. Res.* **111**, E12007 (2006).
14. Yamamoto, S. et al. Olivine-rich exposures in the South Pole-Aitken basin. *Icarus* **218**, 331–344 (2012).
15. Garrick-Bethell, I. & Zuber, M. T. Elliptical structure of the lunar South Pole-Aitken basin. *Icarus* **204**, 399–408 (2009).
16. Vaughan, W. M., Head, J. W., Wilson, L. & Hess, P. C. Geology and petrology of enormous volumes of impact melt on the Moon: a case study of the Orientale basin impact melt sea. *Icarus* **223**, 749–765 (2013).
17. Vaughan, W. M. & Head, J. W. Impact melt differentiation in the South Pole-Aitken basin: some observations and speculations. *Planet. Space Sci.* **91**, 101–106 (2014).
18. Pieters, C. M., Head, J. W., Gaddis, L., Jolliff, B. & Duke, M. Rock types of South Pole Aitken basin and extent of basaltic volcanism. *J. Geophys. Res. Planets* **106**, 28001–28022 (2001).
19. Potter, R. W. K., Collins, G. S., Kiefer, W. S., McGovern, P. J. & Kring, D. A. Constraining the size of the South Pole-Aitken basin impact. *Icarus* **220**, 730–743 (2012).
20. Melosh, H. J. et al. South Pole-Aitken basin ejecta reveal the Moon's upper mantle. *Geology* **45**, 1063–1066 (2017).
21. .Guo, H. & Wu, J. in *Space Science and Technology in China: A Roadmap to 2050* (ed. Guo, H.) **99** (Chinese Academy of Sciences Science Press, Beijing, 2009).
22. US National Research Council. *The Scientific Context for Exploration of the Moon* (National Academies Press, Washington DC, 2007).
23. Moriarty, D. P. et al. Finsen and Alder: a compositional study of lunar central peak craters in the South Pole-Aitken basin. *Lunar Planet. Sci. Conf.* **42**, 2564 (2011).
24. Ling, Z. et al. Correlated compositional and mineralogical investigations at the Chang' E-3 landing site. *Nat. Commun.* **6**, 8880 (2015).
25. Hapke, B. Space weathering from Mercury to the asteroid belt. *J. Geophys. Res. Planets* **106**, 10039–10073 (2001).
26. Pieters, C. M. et al. Space weathering on airless bodies: resolving a mystery with lunar samples. *Meteorit. Planet. Sci.* **35**, 1101–1107 (2000).
27. Klima, R. L., Dyar, M. D. & Pieters, C. M. Near infrared spectra of clinopyroxenes: effects of calcium content and crystal structure. *Meteorit. Planet. Sci.* **46**, 379–395 (2011).
28. Klima, R. L., Pieters, C. M. & Dyar, M. D. Spectroscopy of synthetic Mg-Fe pyroxenes I: spin-allowed and spin-forbidden crystal field bands in the visible and near-infrared. *Meteorit. Planet. Sci.* **42**, 235–253 (2007).
29. Sunshine, J. M., Pieters, C. M. & Pratt, S. F. Deconvolution of mineral absorption bands: an improved approach. *J. Geophys. Res. Solid Earth* **95**, 6955–6966 (1990).
30. Sunshine, J. M. & Pieters, C. M. Estimating modal abundances from the spectra of natural and laboratory pyroxene mixtures using the modified Gaussian model. *J. Geophys. Res. Planets* **98**, 9075–9087 (1993).
31. Nakamura, R. et al. Ultramafic impact melt sheet beneath the South Pole–Aitken basin on the Moon. *Geophys. Res. Lett.* **36**, L22202 (2009).
32. Neumann, G. & Head, J. Geophysical characteristics of Von Kármán crater: Chang/E 4 landing site region. *Lunar Planet. Sci. Conf.* **50**, 2132 (2019).

Acknowledgements This research was funded by the Chang'E-4 mission of CLEP. We thank the team members of the Ground Application and Research System (GRAS), who contributed to data receiving and preprocessing.

Reviewer information *Nature* thanks Rachel Klima and Patrick Pinet for their contribution to the peer review of this work.

Author contributions C.L., D.L., B.L., X.R. and J.L. designed the research, performed data analysis and wrote the manuscript. Z.O. contributed scientific background, geological and geophysical context, and consistency of remote-sensing observation. W.Z., X. Zeng, X.T., X. Zhang and W.C. conducted data preprocessing. H.Z., Y.S. and W.W. helped with data receiving. Z.H., R.X. and R.S. helped with instrument design and data calibration.

Competing interests The authors declare no competing interests.

Additional information
Extended data is available for this paper at https://doi.org/10.1038/s41586-019-1189-0.
Reprints and permissions information is available at http://www.nature.com/reprints.
Correspondence and requests for materials should be addressed to C.L. or X.R. or J.L.
Publisher's note: Springer Nature remains neutral with regard to jurisdictional claims in published maps and institutional affiliations.

METHODS

The VNIS. As one of the four scientific payloads on the Chang'E-4 Yutu-2 rover, the main task of the VNIS is in situ mineral detection on the lunar surface. The technical characteristics of the Chang'E-4 VNIS (Extended Data Table 1) are consistent with those of Chang'E-3[7,33]. The VNIS spectral range is 450–2,400 nm and consists of one hyperspectral imaging detector (VIS/NIR; 450–950 nm) and one single-point spectrometer (SWIR; 900–2,400 nm). The VNIS is mounted on the front of the rover at a height of 0.69 m above the ground and detects the lunar surface at a nominal angle of 45°, leading to an isosceles trapezoid detection area on the surface (height, 20.6 cm and two parallel sides of 13.5 cm and 15.7 cm)[34,35]. The single-point SWIR spectrometer has a circular field of view, the centre of which corresponds to (X98, Y128) of the VIS/NIR image. The radius of the circle covers 53.8 pixels of the VIS/NIR image (pixel size, 25 μm). In addition, the VNIS carries a calibration panel composed of polytetrafluoroethylene.

VNIS data processing and analysis. The VNIS spectral data processing began with level 2B data, which underwent dark-current subtraction, scattering-background correction, flat-field and instrument temperature corrections, and radiometric and geometric calibration[7,33]. First, the radiance data of the VIS/NIR and SWIR bands of CE4_0015 and CE4_0016 were divided by the solar irradiance, multiplied by π, and further divided by the cosine of the incident angle to obtain the reflectance factor, REFF, of the two detection points. Second, for each detection point, the reflectance spectra (450–950 nm) of 9,082 pixels from the circle shown in Fig. 1c, d within the imaged area were averaged to obtain one spectrum (450–950 nm), which was then connected with the point spectrum (900–2,400 nm) measured in the same circular area. However, this process requires the correction of a step artefact caused by the different spectral responses of the two detectors. Considering the small spectral jitter and the stability of the point spectral data, we took the SWIR data as the standard and multiplied the VIS/NIR data by an adjustment factor, which was derived from the ratio of SWIR 900-nm to the VIS-NIR 900-nm reflectance data, to obtain one continuous spectrum. Finally, the continuous spectra were smoothed using the Savitzky–Golay method[24,36] (Fig. 2a) and the spectral continuum was removed using the ENVI software (convex hull fit) (Fig. 2b). After removal of the continuum, the positions of the 1-μm and 2-μm absorption bands of the two spectra were identified through parabola fitting (Extended Data Fig. 2). The results show that the positions of the 1-μm band for CE4_0015 and CE4_0016 are 949.2 nm and 995.1 nm, and those of the 2-μm band are 1,985.9 nm and 1,984.9 nm, respectively. A photometric correction has not yet been performed in this study owing to the lack of a suitable correction model for large phase angles (>90°). However, this does not affect the comparison among CE4_0015, CE4_0016 and CE3_0008 data because of the similar phase angles (~90°) of the three spectra.

Mineral assemblage analysis using MGM deconvolution. MGM was applied to deconvolve the CE4_0015 and CE4_0016 spectra to constrain their mineral composition[30,37]. The software developed by the Reflectance Experiment Laboratory (Relab; http://www.planetary.brown.edu/relab/) was used. The identified absorption-band positions of CE4_0015 and CE4_0016 imply the presence of pyroxene. Both spectra have wide and strong 1-μm absorption but weak 2-μm absorption, resulting in a higher area ratio between the 1-μm and 2-μm bands[33,38,39]. This suggests the presence of a high amount of olivine within the Chang'E-4 landing site in addition to the pyroxene components. However, we cannot rule out the existence of plagioclase. Therefore, we used four different mineral assemblages (LCP + HCP + OL, LCP + HCP + Plag, LCP + Plag, LCP + OL) and different numbers of Gaussian bands (8, 6, 4, 6) to deconvolve the CE4_0015 spectra[24]. The initial parameter settings for MGM are shown in Extended Data Table 2, and Extended Data Fig. 3 shows the MGM modelling results for different mineral assemblages. Generally, the derived 1-μm-band depth ratios of LCP/HCP should be similar to their 2-μm-band depth ratios[30]. Moreover, when olivine is considered in the MGM deconvolution process, the Fo value (the relative content of forsterite in olivine, Fo = {[Mg]/([Mg] + [Fe])}×100, where square brackets denote concentrations in mol%) derived from the three absorption bands of olivine around 1 μm should be consistent[37]. Following these criteria, the best mineral combination is LCP + HCP + OL and its MGM deconvolution result reveals the lowest r.m.s. error (1.97×10^{-3}). We also analysed the statistical significance of the difference between the MGM fit and the observed spectral data for all of these mineral assemblages using two- factor analysis of variance without replication to further evaluate the MGM fitting results. The significance test (see Extended Data Table 3) shows that HCP + LCP + OL has the lowest F value (the value on the F distribution) and the largest P value compared to the other three groups, which means that this mineral assemblage can achieve the best MGM fitting results. The same mineral assemblage (LCP + HCP + OL) was also used to perform MGM deconvolution on CE4_0016, resulting in an r.m.s. error of 1.98×10^{-3}. The initial parameter settings for CE4_0016 are shown in Extended Data Table 4, and the deconvolution result is shown in Fig. 2d.

The content ratio of HCP/LCP can be calculated using their band-depth ratios at 1 μm or 2 μm, which are derived from MGM deconvolution[27,28,30,40,41]. The ratio of the 1-μm-band depth for HCP to the 1.25-μm-band depth for olivine can be used to estimate their relative content[40]. The MGM deconvolution results of the two spectra are shown in Fig. 2c, d, Extended Data Figs. 4, 5. The results show that for CE4_0015 the content ratio LCP:HCP is 81%:19% (1 μm position) and HCP:OL is 17%:83%. Therefore, LCP:HCP:OL is 42%:10%:48%. For CE4_0016, the ratio LCP:HCP is 84%:16% (1 μm position) and HCP/OL is 12%:88%. Thus, LCP:HCP:OL is 38%:7%:55%. According to the relationship between the Fo value and the absorption-band positions of olivine[37] (Extended Data Fig. 5), the derived Fo values for CE4_0015 and CE4_0016 are 57% and 28%, respectively. CE4_0016 has more fayalite than CE4_0015. Currently, we cannot explain the large deviation between the olivine Fo values of these two detection points. In a previous study[40] it was shown that large-grain-size forsterites have absorption characteristics that may mimic the absorption features of fayalite. For olivine of the same composition, the variation in Fo value derived from MGM deconvolution can be up to about 30% when the grain size changes from 45–75 μm to 250–500 μm. Interpretation of the MGM deconvolution results should consider the effect of changing grain size. In this study, we are unable to accurately constrain the grain size distribution of the landing site. Therefore, the Fo value of olivine derived here could be affected by grain size. The difference between the CE4_0015 and CE4_0016 Fo values may not result from the chemical variation of olivine—it may be also due to the changing grain size of the landing site.

Data availability

Reflectance data for CE4_0015 and CE4_0016 are provided in Source Data. The source data for the Chang'E-2 Digital Orthophoto Map and the Chang'E-4 Terrain Camera image (Fig. 1) are available from the Data Publishing and Information Service System of China's Lunar Exploration Program (http://moon.bao.ac.cn). LSCC data are available from LSCC (http://www.planetary.brown.edu/relabdocs/LSCCsoil.html). Datasets generated or analysed during this study are available from the corresponding author upon reasonable request.

33. Liu, B. et al. Data processing and preliminary results of the Chang'E-3 VIS/NIR imaging spectrometer in-situ analysis. *Res. Astron. Astrophys.* **14**, 1578–1594 (2014).
34. Wu, Y. Z. & Hapke, B. Spectroscopic observations of the Moon at the lunar surface. *Earth Planet. Sci. Lett.* **484**, 145–153 (2018).
35. Wu, Y. Z. et al. The absolute reflectance and new calibration site of the Moon. *Astron. J.* **155**, 213 (2018).
36. Savitzky, A. & Golay, M. J. Smoothing and differentiation of data by simplified least squares procedures. *Anal. Chem.* **36**, 1627–1639 (1964).
37. Sunshine, J. M. & Pieters, C. M. Determining the composition of olivine from reflectance spectroscopy. *J. Geophys. Res. Planets* **103**, 13675–13688 (1998).
38. Staid, M. I. et al. The mineralogy of late stage lunar volcanism as observed by the Moon Mineralogy Mapper on Chandrayaan-1. *J. Geophys. Res. Planets* **116**, E00G10 (2011).
39. Besse, S. et al. Compositional variability of the Marius Hills volcanic complex from the Moon Mineralogy Mapper (M^3). *J. Geophys. Res. Planets* **116**, E00G13 (2011).
40. Clénet, H. et al. A new systematic approach using the Modified Gaussian Modal: insight for the characterization of chemical composition of olivines, pyroxenes and olivine-pyroxene mixtures. *Icarus* **213**, 404–422 (2011).
41. Kanner, L. C., Mustard, J. F. & Gendrin, A. Assessing the limits of the Modified Gaussian Model for remote spectroscopic studies of pyroxenes on Mars. *Icarus* **187**, 442–456 (2007).

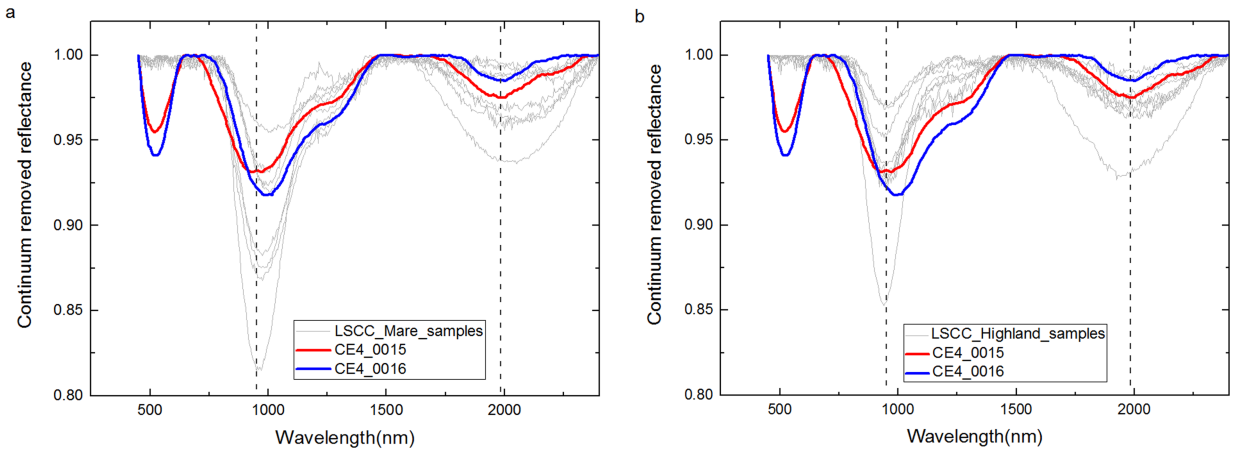

Extended Data Fig. 1 | Spectral comparison between CE4_0015, CE4_0016 and LSCC samples (continuum removed). The red and blue lines represent CE4_0015 and CE4_0016. **a**, Comparison of CE4_0015 and CE4_0016 with mare soil (particle size <45 μm) samples: 10084, 12001, 12030, 15041, 15071, 70181, 71501, 79221. The 1-μm and 2-μm absorption bands of CE4_0015 and the 2-μm absorption band of CE4_0016 (dashed lines) obviously shifts to shorter wavelengths and differ considerably from the spectral features of the mare samples. **b**, Comparison of CE4_0015 and CE4_0016 with highland samples (particle size <45 μm): 14141, 14163, 14259, 14260, 61141, 61221, 62231, 64801, 67461, 67481. The 1-μm and 2-μm absorption bands of CE4_0015 and the 2-μm absorption band (dashed lines) of CE4_0016 resemble those of the highland samples. However, the 1-μm absorption band of CE4_0016 is more similar to that of basaltic soil, which can be attributed to elevated abundance of olivine (see main text).

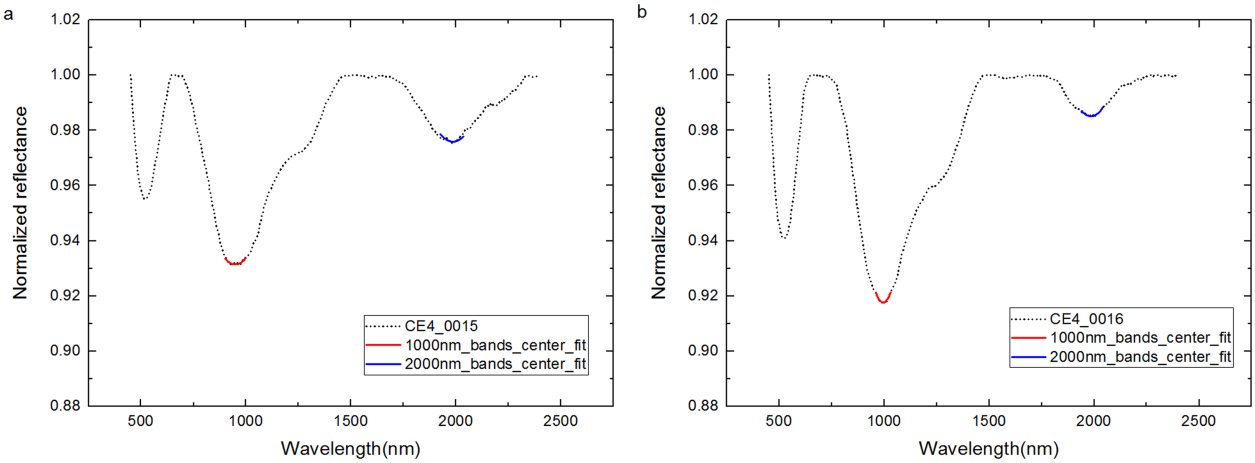

Extended Data Fig. 2 | Parabola-fitting results for CE4_0015 and CE4_0016 1-μm and 2-μm absorption-band positions. a, Reflectance of CE4_0015; the positions of the 1-μm and 2-μm bands are 949.2 nm and 1,985.9 nm, respectively. **b**, Reflectance of CE4_0016; the 1-μm- and 2-μm-band positions are 995.1 nm and 1,984.9 nm, respectively. The 2-μm-band centre assignment is tentative because of its weak absorption. The red and blue lines represent the wavelength ranges used for the parabola fitting of the 1-μm- and 2-μm-band centres, respectively.

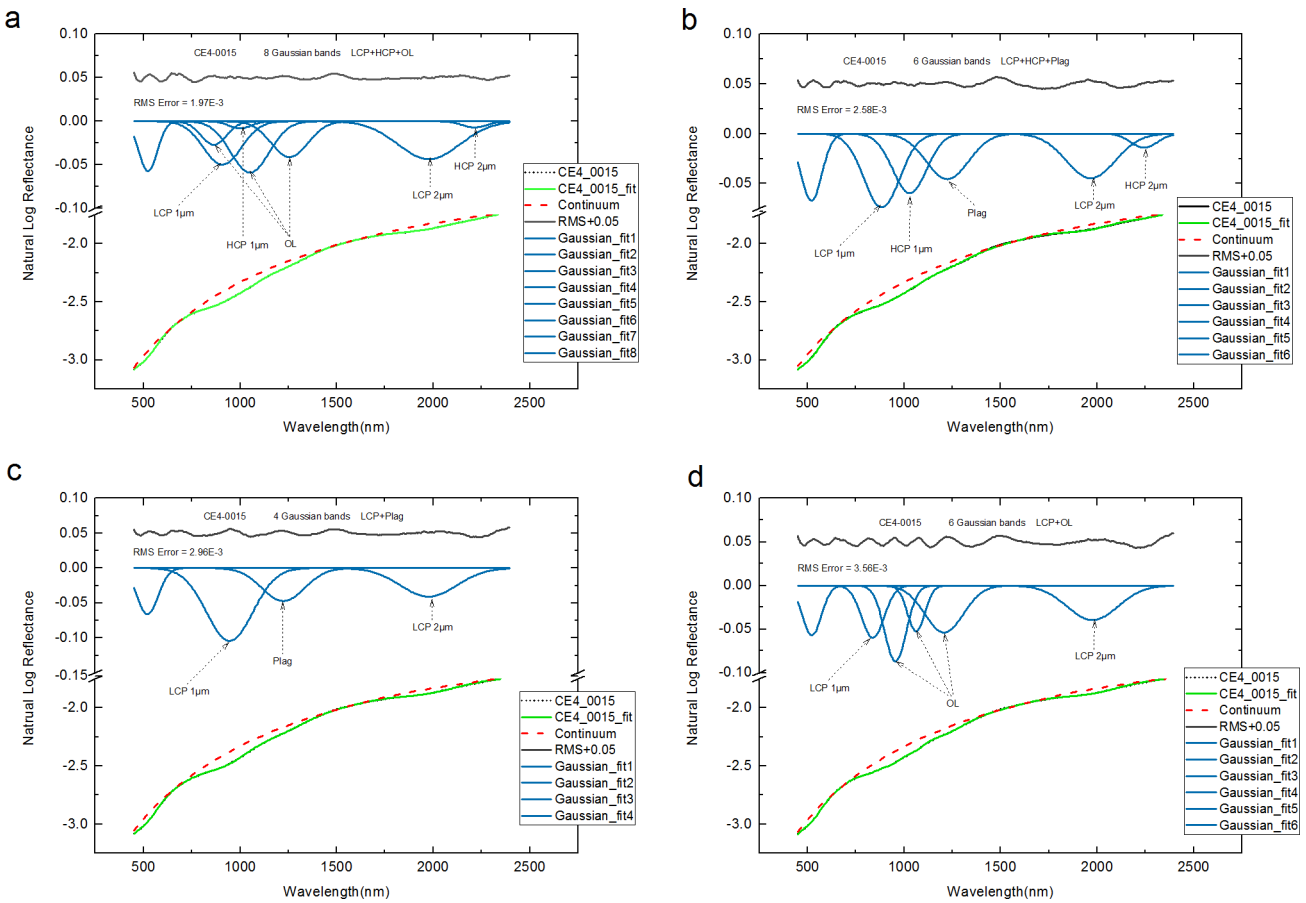

Extended Data Fig. 3 | MGM deconvolution results of CE4_0015 spectra using four different mineral assemblages. a, LCP + HCP + OL. **b**, LCP + HCP + Plag. **c**, LCP + Plag. **d**, LCP + OL.

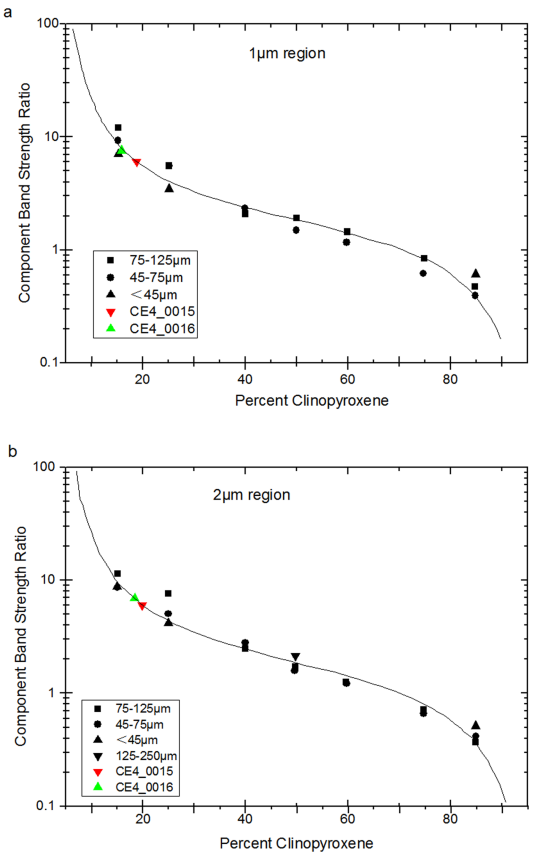

Extended Data Fig. 4 | Content ratio HCP/(HCP + LCP) for CE4_0015 and CE4_0016, calculated by MGM deconvolution. a, 1-μm result: 19% (CE4_0015) and 16% (CE4_0016). **b**, 2-μm results: 20% (CE4_0015) and 18% (CE4_0016). Data are from figure 7 of ref. [30], overlain on calibration lines (solid black line). Solid black symbols represent pyroxene samples of different grain size. The calibration line is defined by the relationship between the MGM-derived band-depth ratio of LCP/HCP and the content ratio of HCP/(HCP + LCP) measured in the laboratory for all grain sizes of the pyroxene samples. The MGM-derived band-depth ratios of LCP/HCP for CE4_0015 (red triangle) and CE4_0016 (green triangle) were projected onto the calibration line to estimate their corresponding content ratio of HCP/(HCP + LCP).

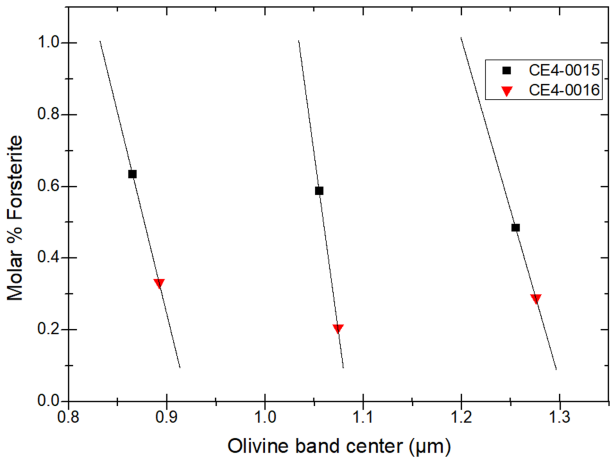

Extended Data Fig. 5 | Molar fraction of forsterite in olivine in CE4_0015 and CE4_0016. The results were derived from VNIS spectra, overlain on calibration lines defined by the relationship between the Fo value and the absorption-band positions of olivine of various compositions (data used to plot the calibration lines are from figure 4 of ref. [37]).

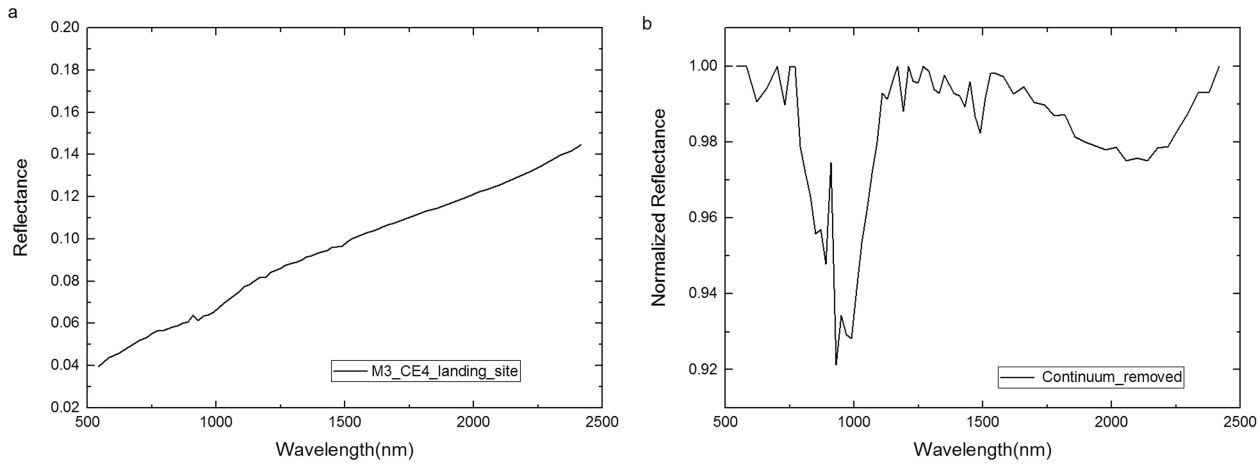

Extended Data Fig. 6 | M^3 reflectance spectrum of Chang'E-4 landing site. a, Average M^3 reflectance spectra obtained using five adjacent pixels with central pixel position (64, 4,927). **b**, Continuum-removed spectrum; 1-μm-band position, 930.1 nm; 2-μm-band position, 2,058.66 nm.

Extended Data Table 1 | Performance characteristics of Chang'E-4 VNIS

Description	Specification	
	VIS/NIR	SWIR
Spectral range（nm）	450~950	900~2400
Spectral resolution（nm）	2.4~6.5	3.6~9.6
Field of view（°）	8.5°*8.5°	Φ3.58°
Effective pixel counts	256*256	1
Bit resolution	10	16
Signal to noise ratio	43（maximum SNR） 33（albedo=0.09, and solar elevation angle=45°）	46（maximum SNR） 31（albedo=0.09, and solar elevation angle=45°）
Detection distance（m）	0.7~1.3	
Power consumption（W）	16.95	
weight（kg）	4.65 (probe part) and 0.48 (electronics part)	
Work modes	Detection mode、calibration mode and dust proofing mode	

SNR, signal-to-noise ratio; *Φ*, circular field of view of SWIR.

Extended Data Table 2 | MGM modelling parameters and errors of CE4_0015 spectra using different mineral components

Continuum fitting parameters		Second-order polynomial: C0 = -3.8E-3;C1 = 1.20223E-3;C2 = -1.8657E-8							
Gaussian fitting Parameters		LCP+HCP+OL		LCP+HCP+Plag		LCP+Plag		LCP+OL	
		Startingparameters	Final parameters	Starting parameters	Final parameters	Starting parameters	Final parameters	Starting parameters	Final parameters
No. of Bands		8	8	6	6	4	4	6	6
Band 1 center		515	523.5	515	520.8	500	521.2	510	523.3
Band 1 width		110	112.5	120	126.9	130	129.3	110	115.7
Band 1 strength		-0.15	-0.06	-0.17	-0.07	-0.17	-0.07	-0.15	-0.06
Band 2 center	OL M1-1	880	864.9	930	885.4	930	946.6	870	838.9
Band 2 width		155	156.1	210	218.1	270	282.5	115	136.8
Band 2 strength		-0.1	-0.03	-0.25	-0.07	-0.25	-0.1	-0.08	-0.06
Band 3 center	LCP	915	909.3	980	1029.6	1300	1224.7	915	956.0
Band 3 width		230	231.0	200	205.3	260	259.7	120	132.4
Band 3 strength		-0.25	-0.05	-0.11	-0.06	-0.02	-0.05	-0.25	-0.09
Band 4 center	HCP	1000	1001.5	1290	1225.2	1980	1977.6	1050	1063.0
Band 4 width		135	134.9	260	258.5	340	343.3	80	105.6
Band 4 strength		-0.15	-0.008	-0.02	-0.05	-0s.1	-0.04	-0.08	-0.05
Band 5 center	OL M2	1050	1052.1	1980	1968.2			1250	1208.5
Band 5 width		235	234.6	290	299.2			225	235.6
Band 5 strength		-0.1	-0.06	-0.1	-0.04			-0.1	-0.05
Band 6 center	OL M1-2	1250	1257.2	2250	2244.5			1950	1976.7
Band 6 width		225	225.0	160	161.3			300	310.4
Band 6 strength		-0.15	-0.04	-0.1	-0.01			-0.1	-0.04
Band 7 center	LCP	1985	1978.9						
Band 7 width		380	380.4						
Band 7 strength		-0.1	-0.04						
Band 8 center	HCP	2215	2215.8						
Band 8width		150	149.9						
Band 8 strength		-0.07	-0.007						
RMS Error		1.97E-3		2.58E-3		2.96 E-3		3.56 E-3	

RMS, root mean square.

Extended Data Table 3 | Significance test for MGM deconvolution of CE4_0015

Source of variation	F	P-value	F crit
fit-0015_HCP+LCP+OL	4.94774E-07	0.999439	3.865475
fit_0015_LCP+OL	0.000416932	0.98372	3.865475
fit-0015_LCP+plag	0.000215657	0.988291	3.865475
fit_0015_HCP+LCP+Plag	0.001506455	0.969059	3.865475

'F crit' is the critical *F* value, which can be obtained from the *F* distribution table.

Extended Data Table 4 | MGM modelling parameters and errors for CE4_0016

Continuum fitting parameters		Second-order polynomial: C0 = -3.8E-3;C1 = 1.20223E-3;C2 = -1.8657E-8							
Gaussian fitting Parameters		LCP+HCP+OL		LCP+HCP+Plag		LCP+Plag		LCP+OL	
		Startingparameters	Final parameters	Starting parameters	Final parameters	Starting parameters	Final parameters	Starting parameters	Final parameters
No. of Bands		8	8	6	6	4	4	6	6
Band 1 center		515	523.5	515	520.8	500	521.2	510	523.3
Band 1 width		110	112.5	120	126.9	130	129.3	110	115.7
Band 1 strength		-0.15	-0.06	-0.17	-0.07	-0.17	-0.07	-0.15	-0.06
Band 2 center	OL M1-1	880	864.9	930	885.4	930	946.6	870	838.9
Band 2 width		155	156.1	210	218.1	270	282.5	115	136.8
Band 2 strength		-0.1	-0.03	-0.25	-0.07	-0.25	-0.1	-0.08	-0.06
Band 3 center	LCP	915	909.3	980	1029.6	1300	1224.7	915	956.0
Band 3 width		230	231.0	200	205.3	260	259.7	120	132.4
Band 3 strength		-0.25	-0.05	-0.11	-0.06	-0.02	-0.05	-0.25	-0.09
Band 4 center	HCP	1000	1001.5	1290	1225.2	1980	1977.6	1050	1063.0
Band 4 width		135	134.9	260	258.5	340	343.3	80	105.6
Band 4 strength		-0.15	-0.008	-0.02	-0.05	-0s.1	-0.04	-0.08	-0.05
Band 5 center	OL M2	1050	1052.1	1980	1968.2			1250	1208.5
Band 5 width		235	234.6	290	299.2			225	235.6
Band 5 strength		-0.1	-0.06	-0.1	-0.04			-0.1	-0.05
Band 6 center	OL M1-2	1250	1257.2	2250	2244.5			1950	1976.7
Band 6 width		225	225.0	160	161.3			300	310.4
Band 6 strength		-0.15	-0.04	-0.1	-0.01			-0.1	-0.04
Band 7 center	LCP	1985	1978.9						
Band 7 width		380	380.4						
Band 7 strength		-0.1	-0.04						
Band 8 center	HCP	2215	2215.8						
Band 8width		150	149.9						
Band 8 strength		-0.07	-0.007						
RMS Error		1.97E-3		2.58E-3		2.96 E-3		3.56 E-3	